Improved Nowcasts by Blending Extrapolation and Model Forecasts

YUNSUNG HWANG

Cooperative Institute of Mesoscale Meteorological Studies, and School of Meteorology, University of Oklahoma, and National Severe Storms Laboratory, Norman, Oklahoma

ADAM J. CLARK

Cooperative Institute of Mesoscale Meteorological Studies, University of Oklahoma, and National Severe Storms Laboratory, Norman, Oklahoma

VALLIAPPA LAKSHMANAN

Climate Corporation, Seattle, Washington

STEVEN E. KOCH

School of Meteorology, University of Oklahoma, and National Severe Storms Laboratory, Norman, Oklahoma

(Manuscript received 30 April 2015, in final form 10 July 2015)

ABSTRACT

Planning and managing commercial airplane routes to avoid thunderstorms requires very skillful and frequently updated 0–8-h forecasts of convection. The National Oceanic and Atmospheric Administration's High-Resolution Rapid Refresh (HRRR) model is well suited for this purpose, being initialized hourly and providing explicit forecasts of convection out to 15 h. However, because of difficulties with depicting convection at the time of model initialization and shortly thereafter (i.e., during model spinup), relatively simple extrapolation techniques, on average, perform better than the HRRR at 0–2-h lead times. Thus, recently developed nowcasting techniques blend extrapolation-based forecasts with numerical weather prediction (NWP)-based forecasts, heavily weighting the extrapolation forecasts at 0–2-h lead times and transitioning emphasis to the NWP-based forecasts at the later lead times. In this study, a new approach to applying different weights to blend extrapolation and model forecasts based on intensities and forecast times is applied and tested. An image-processing method of morphing between extrapolation and model forecasts to create nowcasts is described and the skill is compared to extrapolation forecasts and forecasts from the HRRR. The new approach is called salient cross dissolve (Sal CD), which is compared to a commonly used method called linear cross dissolve (Lin CD). Examinations of forecasts and observations of the maximum altitude of echo-top heights $\geq$18 dBZ and measurement of forecast skill using neighborhood-based methods shows that Sal CD significantly improves upon Lin CD, as well as the HRRR at 2–5-h lead times.

1. Introduction

Federal Aviation Administration (FAA) Operations Network (OPSNET) data show that more than 70% of the National Airspace System (NAS) reportable delays are contributed by convective weather (Sheth et al. 2013). Air traffic is routed around anticipated locations of convective weather systems, forcing aircraft to take large deviations. Accurate nowcasts are, therefore, critical to reducing the number of such delays. While the strategic time frame for flight operations is only 8 h, longer-term flight planning requires up to 12-h forecasts of variables containing information on convection such as echo-top heights and vertically integrated liquid (VIL) (Robinson et al. 2008; Pinto et al. 2010).

The focus of recent research in providing support for flight planning has been on developing improved weather products and making better use of probabilistic data, which benefits various participants in air traffic

Corresponding author address: Yunsung Hwang, School of Meteorology, University of Oklahoma, 120 David L. Boren Blvd., No. 5900, Norman, OK 73072.
E-mail: yunsung.hwang@ou.edu

DOI: 10.1175/WAF-D-15-0057.1

management (Fahey et al. 2006). Other research has focused on operational concepts for managing strategic traffic flow, including examination of how improved weather data can aid traffic management initiatives efficiently (Song et al. 2008).

For short-term prediction of convection for route-planning applications, frequently updating high-resolution forecasts of convection are needed (i.e., nowcasts). To address this need, since about the early 1990s, various nowcasting techniques have been developed that rely on extrapolation (EXT) of observed convection as depicted by radar-derived fields (Dixon and Wiener 1993; Li et al. 1995; Germann and Zawadzki 2002, 2004; Mandapaka et al. 2012). Although oftentimes quite skillful at 1–2-h lead times, the extrapolation-based methods suffer from the obvious shortcoming that they are not able to depict rapidly changing conditions associated with processes such as convection initiation, dissipation, and changing intensities and movements. For changing conditions, a rapidly updated numerical weather prediction (NWP) model with high enough resolution to provide explicit forecasts of convection is necessary (Stratman et al. 2013).

To test NWP model forecasts for nowcasting applications, several recent studies have compared the forecast skill of NWP models to extrapolation-based methods at very short lead times. For example, Mandapaka et al. (2012) compared precipitation forecasts from an algorithm known as the McGill Algorithm for Precipitation Nowcasting by Lagrangian Extrapolation (MAPLE; Germann and Zawadzki 2002) to high-resolution NWP-based forecasts from the Consortium for Small-scale Modeling (COSMO) model (COSMO2; http://cosmo-model.org). They found that on average the MAPLE forecasts had higher skill during the first 2.5 h of the forecast, after which the COSMO2 forecasts performed better. Similarly, examining precipitation forecasts, Lin et al. (2005) found that extrapolation-based predictions were more skillful than four different NWP models, on average, up to about 6-h lead times. The lower skill during the first few hours of the NWP-based predictions occurred because of difficulties in depicting small-scale convective features in their model initial conditions, and then correctly evolving these features (i.e., the model ''spinup'' problem). The crossover time (i.e., when the NWP-based forecasts become better) is earlier in the Germann and Zawadzki (2002) study because they used a more advanced NWP system with a more sophisticated data assimilation scheme that assimilated radar-derived rainfall fields. In theory, as sophisticated high-resolution data assimilation methods continue to improve, NWP-based forecasts may eventually become more skillful than extrapolation-based methods at all lead times. However, while the extrapolation methods remain more skillful at short lead times, seamless 0–8-h predictions may be obtained by blending extrapolation with NWP-based forecasts, with the extrapolation forecasts heavily weighted during the first few hours and the heavier weights transitioning to the NWP-based forecasts at later lead times.

To address the nowcasting problem using this blending approach, the FAA collaborated with the Massachusetts Institute of Technology's Lincoln Laboratory (MIT LL), the National Center for Atmospheric Research's (NCAR) Research Applications Laboratory (RAL), and the National Oceanic and Atmospheric Administration/Earth Systems Research Laboratory/Global Systems Division (NOAA/ESRL/GSD) to develop a system known as Consolidated Storm Prediction for Aviation (CoSPA; Wolfson et al. 2008; Dupree et al. 2009). CoSPA was aimed at providing information by blending extrapolation-based forecasts and NWP-based forecasts for lead times up to 8 h. The High-Resolution Rapid Refresh (HRRR; http://ruc.noaa.gov/hrrr/) model, an hourly updated 3-km grid spacing convection-permitting modeling system, developed by NOAA/ESRL/GSD that became operational on 30 September 2014, was utilized as the model forecast. The blending method of CoSPA consists of three steps: 1) calibration of the HRRR data to remove intensity biases, 2) application of a spatial correction to align the HRRR fields with observations, and 3) weighted averaging of the extrapolation and HRRR fields (Pinto et al. 2010).

The method of obtaining weighted averages for blending in CoSPA is based on applying time-varying weights to the extrapolation and HRRR fields. The extrapolation has more weight (close to 1) at the shorter lead times and decreases gradually at the longer lead times (approaching 0). The calibration and the spatial offsets are applied based on the most up-to-date radar mosaic. Pinto et al. (2010) provide additional details on the blending procedure used in CoSPA, as well as verification results for a prototype version of CoSPA during the summers of 2008 and 2009.

Comparing to extrapolation, as well as raw and calibrated HRRR forecasts, Pinto et al. (2010) find that the forecast skill of CoSPA, as measured by the critical success index (CSI), follows that of extrapolation during the first 2–3 h and then converges toward the skill of the HRRR during the last 6–8 h. During forecast hours 3–5, which was when the model skill began to exceed that of extrapolation, the margin by which the skill of CoSPA forecasts exceeded the skill of the next most skillful forecast was highest. Similar results from application of CoSPA during July 2012 can be found in Sun et al. (2014).

Although the blending method used in CoSPA shows promising results, biases near 0.6 within the 3–4-h forecast period indicate a systematic underprediction in the areal coverage of convection during this time. This systematic underprediction can likely be partially explained by the fact that weights are close to 0.5 for both extrapolation and HRRR fields during this time. Thus, in the case of slight displacements between areas of forecast convection in the HRRR and extrapolation fields after spatial correction, the fields would be reduced by half, giving lower overall values in two different locations.

The purpose of this study is to address this underestimation problem using a new blending approach that considers intensity in addition to forecast lead time in the computation of weights. The new blending approach is compared to one in which weights are only dependent on forecast time. Although this time-weighted-only blending approach is less sophisticated than that used in CoSPA (e.g., no attempts are made to correct for the intensity biases of the HRRR forecasts), the comparisons with our newly developed blending approach should serve as a useful proof of concept for application in more advanced nowcasting systems.

The technique to apply different weights based on time and intensities is described and its results are compared to that of a time-weighted-only averaging in section 2 along with a description of the data and our methodology. The results are discussed in section 3. Finally, summary and ideas for future work are presented in section 4.

2. Data and methodology

a. Dataset

In this study, forecasts and observations of 18-dBZ echo-top heights are examined, which are defined as the maximum altitude at which reflectivity exceeds 18 dBZ. The observed echo-top heights are estimated from the Weather Surveillance Radar-1988 Doppler (WSR-88D) data using the highest elevation angle that detects reflectivity over 18 dBZ (Lakshmanan et al. 2013). Echo-top heights were chosen for examination because they are one of the parameters that determine the availability of a flight route in recently developed convective weather avoidance models (Matthews and DeLaura 2010; Sheth et al. 2013). For verification purposes, 18-dBZ echo-top heights computed from the WSR-88D network covering the contiguous United States (CONUS) are used as truth. Four different sets of 8-h forecasts are evaluated, which are all initialized at 1800 UTC. This particular initialization time was chosen because it is a few hours before the typical maximum in the diurnal cycle of convection and, thus, precedes by a few hours the largest potential impacts on flight routing. Forecasts on 24 days during the period from 15 May to 13 June 2013 were examined (the dates 20, 28, and 29 May and 4 and 7 June were excluded because of missing data). The four forecasts consisted of 1) the HRRR, 2) extrapolated observations, 3) a blending of extrapolated observations and the HRRR [linear cross dissolve (Lin CD)], and 4) another blending of extrapolated observations and the HRRR [salient cross dissolve (Sal CD)]. Details on the four forecasts are discussed in the following sections.

b. HRRR

The HRRR is a convection-allowing model, which generates convection without convective parameterization, covering the CONUS with 3-km grid spacing and nested within the parent model domain of the 13-km grid spacing Rapid Refresh (RAP; Brown et al. 2011; Weygandt et al. 2011) model. The RAP provides initial and boundary conditions and assimilates radar reflectivity observations through a diabatic digital filter initialization (Huang and Lynch 1993). The HRRR is based on the Advanced Research version of the Weather Research and Forecasting (WRF) Model (ARW; Skamarock et al. 2008) with the following WRF physics options: 1) the Goddard shortwave radiation scheme (Chou and Suarez 1994), 2) the Rapid Radiative Transfer Model longwave radiation scheme (Mlawer et al. 1997), 3) the RUC Smirnova land surface model (Smirnova et al. 1997), 4) the Mellor–Yamada–Nakanishi–Niino (MYNN) boundary layer parameterization (Nakanishi and Niino 2004), and 5) the Thompson mixed-phase microphysics scheme (Thompson et al. 2008).

The RAP and HRRR assimilate data hourly using the Gridpoint Statistical Interpolation analysis system (GSI). The HRRR utilizes 3-km data assimilation to include detailed observational information using GSI. During a preforecast hour, observed radar reflectivities replace latent heating fields for the HRRR at 15-min intervals. Moreover, at the beginning of the forecast, a 3-km nonvariational cloud analysis and hydrometeor analysis from radar reflectivities are used to obtain additional information about rain and snow mixing ratios.

c. Extrapolated observations

The high spatial and temporal resolution of weather radar data has enabled the development of several nowcasting techniques based on extrapolation methods (Mandapaka et al. 2012). In these methods, the movement of storm cells is typically estimated by matching

radar echoes between two successive radar images. A storm cell is typically defined as a region of reflectivity that exceeds a threshold (usually 35 or 40 dBZ). Examples of tracking and extrapolation algorithms found in the literature include Continuity of Tracking Radar Echoes by Correlation vectors (COTREC; Li et al. 1995), which used variational methods (Sasaki 1958, 1970) to skillfully predict the movement of storm cells 20 min in advance. The Thunderstorm Identification, Tracking, Analysis, and Nowcasting (TITAN; Dixon and Wiener 1993) system was created to optimally match storm cells successive radar images using a linear programming optimization approach called the Hungarian method. MAPLE (Germann and Zawadzki 2002, 2004) applies variational approaches to provide improved extrapolation.

For extrapolation forecasts, we used the segmotion algorithm that is implemented in the Warning Decision Support System–Integrated Information (WDSS-II; Lakshmanan et al. 2006). In this technique, thunderstorms are identified at different scales using the extended watershed approach (Lakshmanan et al. 2009). The image is flooded starting from the global maximum. The flooding level is slowly decreased so that flooding can proceed at lower and lower levels and the entire area covered by water flowing from a single maximum to a predetermined size (this size varies by scale) forms a thunderstorm. Storms identified in consecutive images are associated based on a greedy optimization algorithm (Lakshmanan and Smith 2010) that tries to optimize the match based on projected storm location and a cost function based on continuity of the maximum value. The motion vector derived from storm associations is interpolated onto the full grid using an inverse distance weighting scheme (Lakshmanan et al. 2003). These motion vectors, one for each scale, are then matched to the size of the objects being extrapolated and the time period of extrapolation and used to extrapolate the current echo-top grid into future time steps.

d. Image morphing

In the image-processing literature, creating intermediate images to provide a smooth transition between a pair of images is called morphing. Morphing consists of three image-processing steps: warping, cross dissolving, and unwarping. Because the same entities in the two images may be slightly displaced, the process of warping attempts to align the objects in the two fields. This is typically done through coordinate transformation by choosing the coordinate transformation at which a cost function is minimized. The cost function balances two concerns: that the warping is as small as possible while the difference between the warped version of the first image and the second image is also as small as possible.

The second image-processing step (cross dissolving) is intended to blend the warped version of the first image with the second image with different weights chosen to obtain a series of intermediate images. For example, an intermediate image that is some fraction w of the way ($w < 1$) between the two images may be obtained by assigning a weight w to each pixel in the warped version of the first image and a weight $(1 - w)$ to the corresponding pixel in the second image. Such a linear weighting scheme is not the only possible choice. In this paper, we will employ a saliency-based weighting scheme (discussed later).

The third step is to unwarp the blended image to add back the alignment difference between the pair of images being morphed. This is achieved by applying a weighted inverse of the warping function to the blended image. Thus, if the coordinate transform to warp the first image to the second was $f(x, y)$, the transformation applied to the blended image is $(1 - w)f^{-1}(x, y)$, where w is the weight of the first image in the blended image.

With an appropriately chosen warping function, it is possible to simplify the process above into two steps: 1) warp the first image by $wf(x, y)$ and the second image by $(1 - w)f^{-1}(x, y)$ and 2) cross dissolve the two warped images to obtain the morphed image.

1) LINEAR CROSS DISSOLVE

Linear cross dissolve is a commonly employed blending method that computes the weighted average of two aligned images pixel by pixel. For example, if one tries to combine two images, I_1 (the extrapolation) and I_2 (the model forecast), the cross dissolve of the images $C(x, y)$ can be represented as

$$C(x, y) = wI_1(x, y) + (1 - w)I_2(x, y), \qquad (1)$$

where $I_1(x, y)$ is the intensity of the pixel (x, y) in the first image and $I_2(x, y)$ is used for the second image. Assuming that there are six time steps (0, 1, 2, 3, 4, and 5 h) between I_1 and I_2, at 0 h, the $C(x, y)$ is the same as I_1 since $w = 1$ and $1 - w = 0$. At 3 h, $C(x, y) = 0.6[I_1(x, y)] + 0.4[I_2(x, y)]$ gives slightly more weight to I_1. For morphing extrapolation and model fields, w for a linear cross dissolve is shown in Fig. 1a and $1 - w$ in Fig. 1b. It should be noted that blending weights are independent of the intensities $I_1(x, y)$ and $I_2(x, y)$.

For linear cross dissolve, the same weights are applied to images at a certain fraction of time for all intensities. Essentially, features from I_1 fade out as features from I_2 fade in. Features present in both images fade from their presentation as in I_1 to their presentation as in I_2.

Idealized examples of linear cross dissolve for a line of discrete storm cells are shown in Fig. 2. There are six time steps (0, 1, 2, 3, 4, and 5 h) of three convective cells

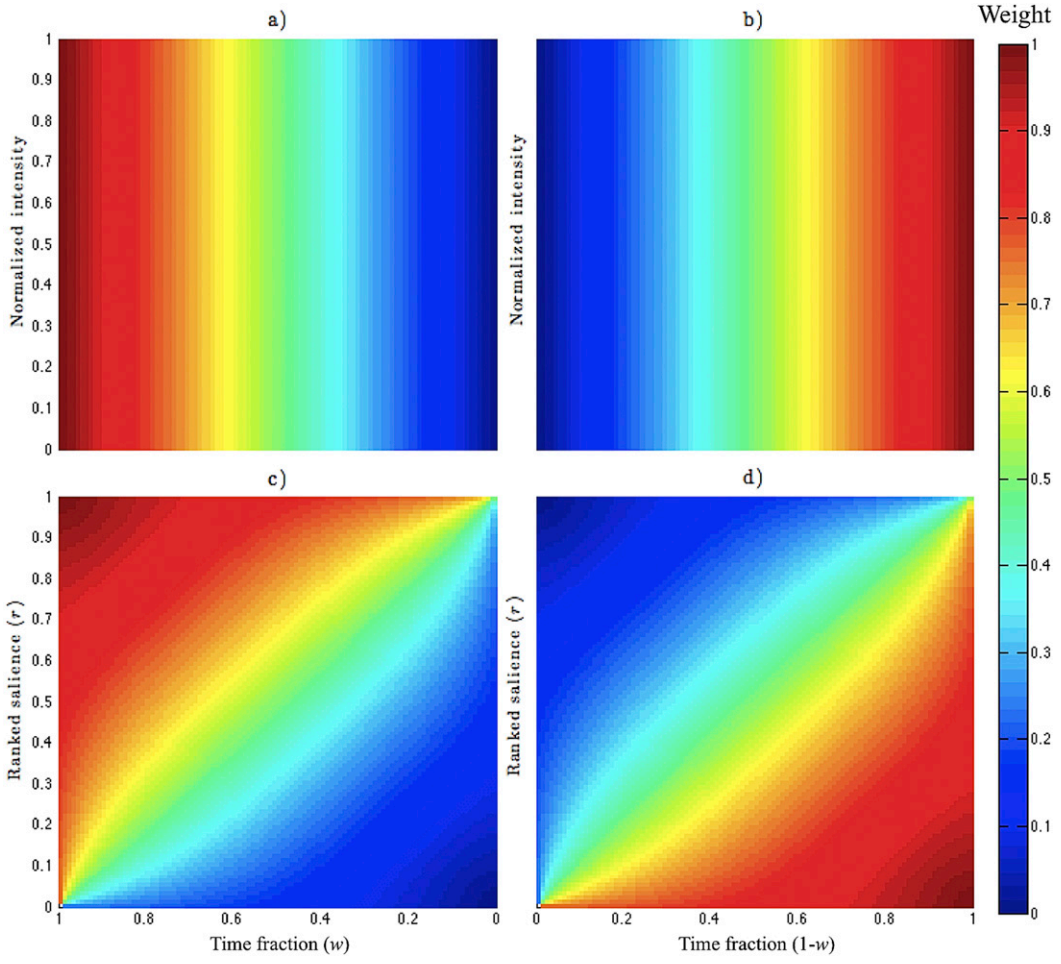

FIG. 1. (a) Lin CD weights for EXT. Weights start at 1 regardless of intensity at 0 h and steadily decrease to 0 at max forecast length. (b) Lin CD weights for HRRR. Weights start at 0 regardless of intensity at 0 h and steadily increase to 1 at max forecast length. (c) Sal CD weights for EXT. The weight of high-intensity pixels (ranked saliency, $r = y$ axis, ~1) remains high throughout the time period whereas low-intensity pixels are dampened more quickly. (d) Sal CD weights for HRRR. The high-intensity pixels (r = ~0) remain high throughout the time period.

in the illustration. The cells are moving to the east at a constant speed as shown in Figs. 2a–f. The top cell has not developed at 0 h but develops at 1 h and increases in intensity until 5 h. The center cell decreases in intensity throughout the idealized forecast period while the bottom cell maintains constant intensity. Extrapolation captures only the center and bottom cells from the observation at 0 h and extrapolates them to the east without changing the intensities. The bottom cell is well captured by extrapolation because it is unchanging in time. However, the change in intensity of the center cell is not captured by the extrapolation. On the other hand, it is not possible to extrapolate the top cell since it was not present in the observations at 0 h. In the illustration, it is assumed that the model forecast simulates only the top and the bottom cells, and with lower intensities.

The blend of the extrapolation and model forecast using Lin CD is shown in Figs. 2s–x. Extrapolated images are weighted higher than the model forecasts close to the beginning of the forecast time and the opposite weighting is employed approaching the end of the forecast time. Lin CD captures all three cells even as the extrapolation and model forecast depict only two cells each. However, the top and center cells tend to have weaker intensities compared to that of the observation. For example at 2 h ($w = 0.6$ and $1 - w = 0.4$) only the center cell is present in the extrapolated image, and, therefore, the intensity in Lin CD is decreased to 60% of the original values. Similarly, the top cell in Lin CD at 2 h obtains 40% of the model forecast intensity at the same time step. As exemplified above, Lin CD is simple and computationally efficient. However, Lin CD

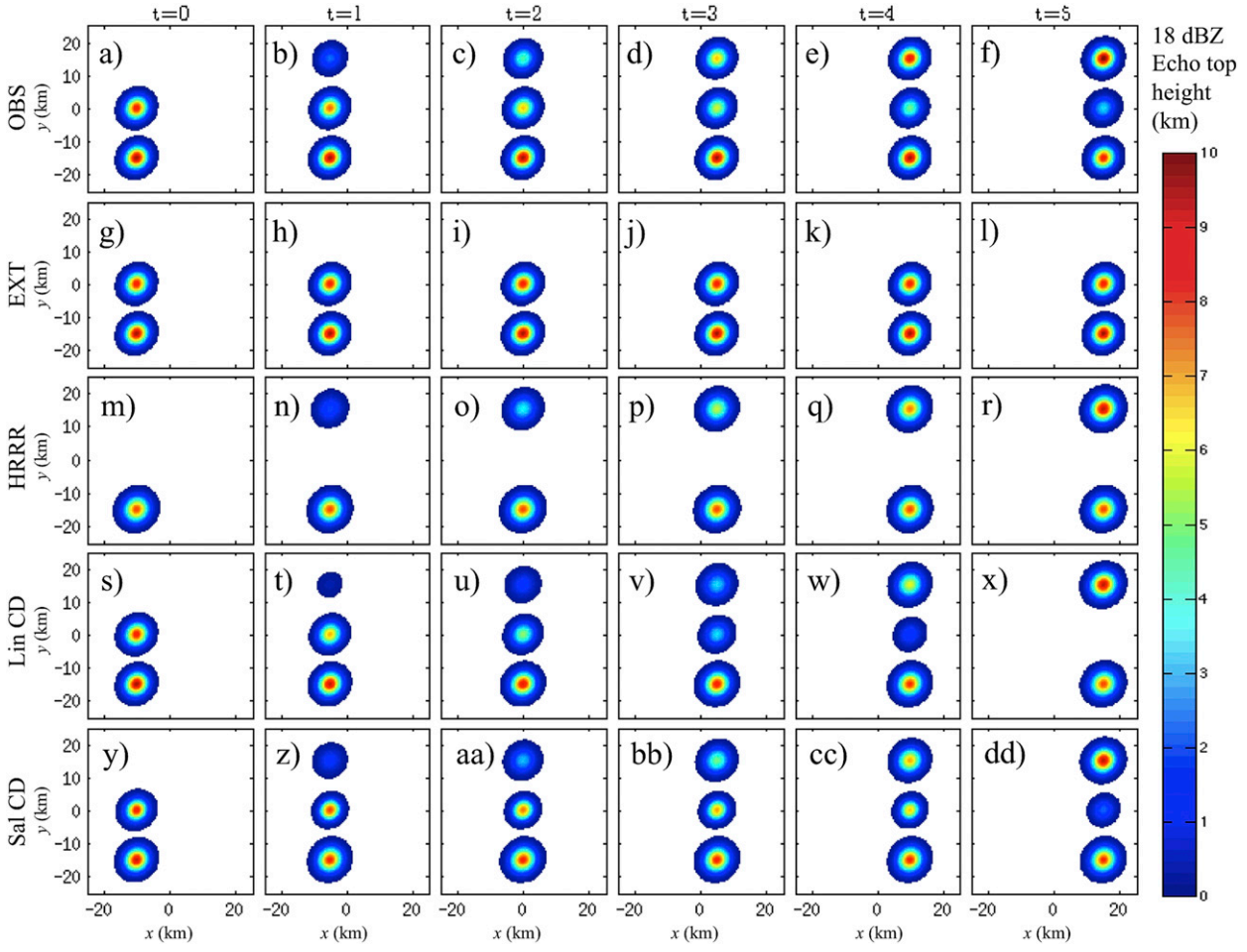

FIG. 2. Illustration of the different forecast methods for an idealized sequence of forecasts and observations at a line of discrete storm cells. (a)–(f) Observed 18-dB*Z* echo-top heights at forecast hours 0–6. (g)–(l) As in (a)–(f), but for idealized forecasts from EXT. (m)–(r) As in (a)–(f), but for idealized forecasts from HRRR. (s)–(x) As in (a)–(f), but for idealized forecasts from Lin CD. (y)–(dd) As in (a)–(f), but for idealized forecasts from Sal CD.

dampens the amplitude of features by applying constant weights.

2) SALIENT CROSS DISSOLVE

A method of maintaining the features from multiple images considering the saliency (or importance) of different intensities was developed and applied to image blending (Grundland et al. 2006). The goal of that study was to preserve color and contrast while blending multiple images with different resolutions. Salience contrast and color in that study refer to the informative aspects of the image as far as human vision is concerned. In this study, we define salience as the locations of strong cells (in terms of normalized intensities). Consequently, the composite image using saliency-based cross dissolve is defined using the following equation from Grundland et al. (2006):

$$S(x,y) = w_s[w, r(x,y)]I_1(x,y) + \{1 - w_s[1 - w, r(x,y)]\}I_2(x,y), \quad (2)$$

where S is composite image of I_1 and I_2, and w_s is a two-dimensional function of weight and the ranked salience $r(x, y)$, where w_s is calculated using

$$w_s(w,r) = \frac{1}{2}\left[\frac{wr}{wr + (1-w)(1-r)} + \frac{\sqrt{r^2 + w^2}}{\sqrt{r^2 + w^2} + \sqrt{(1-r)^2 + (1-w)^2}}\right]. \quad (3)$$

Compared to the linear weights of Figs. 1a and 1b, w_s allows the blended product to preserve pixel intensities

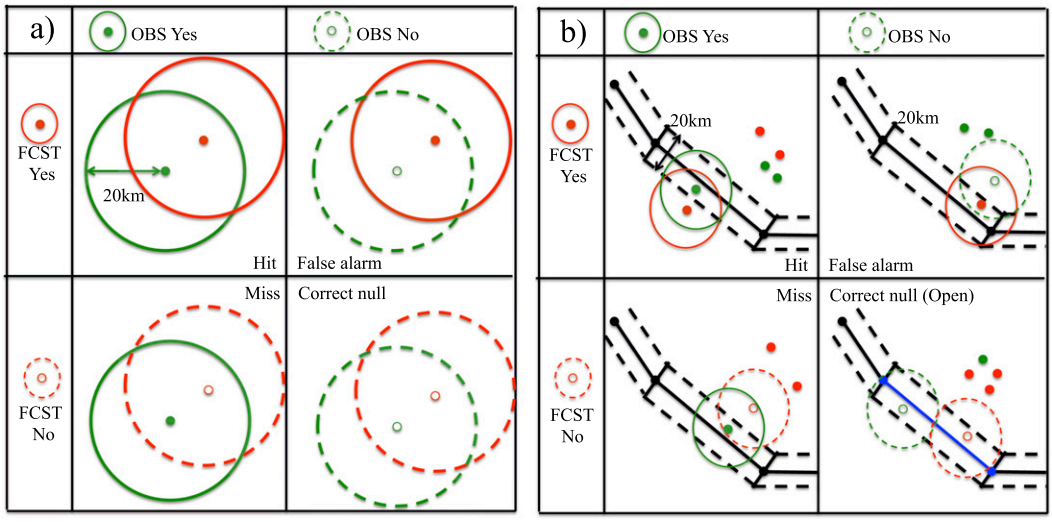

FIG. 3. (a) Schematic of the NE method. Filled green dots show locations of observed 18-dBZ echo-top heights exceeding 9 km. The green circles of 20-km radius (from filled green dots) determine hits if locations from 18-dBZ echo-top heights exceed 9 km based on forecasts (EXT, HRRR, Lin CD, and Sal CD). These are the filled red dots inside the green circles. In contrast, unfilled dots depict missing locations either in observations (green) or forecasts (red). Dotted circles of 20-km radius from unfilled green and red dots are ranges where there should be locations if the 18-dBZ echo-top height exceeding 9 km either from observation or forecasts are to be positively scored. (b) Schematic of the route-based segments method. The circles are the same as those in the NE method, but only locations inside the route segments (rectangular regions in the black contours with a width of 20 km) estimated using two waypoints (filled black dots) are evaluated. If there are no locations with 18-dBZ echo-top heights exceeding 9 km inside the route segments, the segment is opened as indicated by the blue line for the correct null (open).

with time if they are strong enough based on the r value (see Figs. 1c,d). Using Grundland et al. (2006), $r(x, y)$ is calculated as

$$r(x,y) = \Phi[N_1(x,y) - N_2(x,y)], \tag{4}$$

where $\Phi(x)$ is a cumulative density function (i.e., $\Phi\{\mathrm{Min}[N_1(x,y)-N_2(x,y)]\}=0$ and $\Phi\{\mathrm{Max}[N_1(x,y)-N_2(x,y)]\}=1$) and $N_n(x,y)$ is the normalized intensity of the image, $N_n(x,y)=N_n(x,y)/\mathrm{Max}[N_n(x,y)]$, where n is the number of images ($n=1$ and 2 in this study).

If the strongest cell is only in $I_1(x, y)$ and not in $I_2(x, y)$ at a location (x, y), then $\Phi[N_1(x, y) - N_2(x, y)]$ is close to 1 because $N_1(x, y)$ is close to 1 and $N_2(x, y)$ is close to 0. In contrast, if the strongest cell is only in $I_2(x, y)$, then $\Phi[N_1(x, y) - N_2(x, y)]$ is close to 0 because $N_1(x, y) - N_2(x, y)$ is close to -1 at the location (x, y). It should be noted that $r(x, y)$ is not the intensity itself. We use $r(x, y)$ to show how close the pixel is to the maximum intensity difference of $N_1(x, y) - N_2(x, y)$ [i.e., $r(x, y) = 1$] or the minimum intensity difference of $N_1(x, y) - N_2(x, y)$ [i.e., $r(x, y) = 0$].

The composite image $S(x, y)$ of the extrapolation and model forecasts using Sal CD is shown in Figs. 2y–dd. Sal CD simulates three cells better than Lin CD especially at 2 ($w = 0.6$ and $1 - w = 0.4$) and 3 h ($w = 0.4$ and $1 - w = 0.6$) because the higher intensities in the observations are retained. For example at 2 h, the center cell has high r close to 1, where w_s would be close to 0.9 (the point where $w = 0.6$ and $r = 1$ in Fig. 1c) and the bottom cell has low r close to 0, where $1 - w_s$ would be close to 0.9 (the point where $1 - w = 0.4$ and $r = 0$ in Fig. 1d). Thus, both the middle and bottom cells keep high intensities in Sal CD. Additionally, the center cell is shown in Sal CD at 5 h while it is not shown in Lin CD at 5 h. It is possible to obtain the center cell even when the weight for I_1 is zero at 5 h because w_s can be 0.5 if the intensity is close to 1.

e. Statistical evaluation

We employed two methods to evaluate the forecasts over the 24 days that data were available. The first evaluation method is the neighborhood (NE) method with a radius of 20 km. Deep moist convection is defined as 18-dBZ echo-top heights ≥9 km (≈30 000 ft). The lowest echo-top height considered dangerous for an airplane is typically 25 000 ft (Matthews and DeLaura 2010). However, commercial airplanes usually fly at 30 000–40 000 ft, which was why 9 km was chosen as the threshold for convection in this study. Utilizing the neighborhood

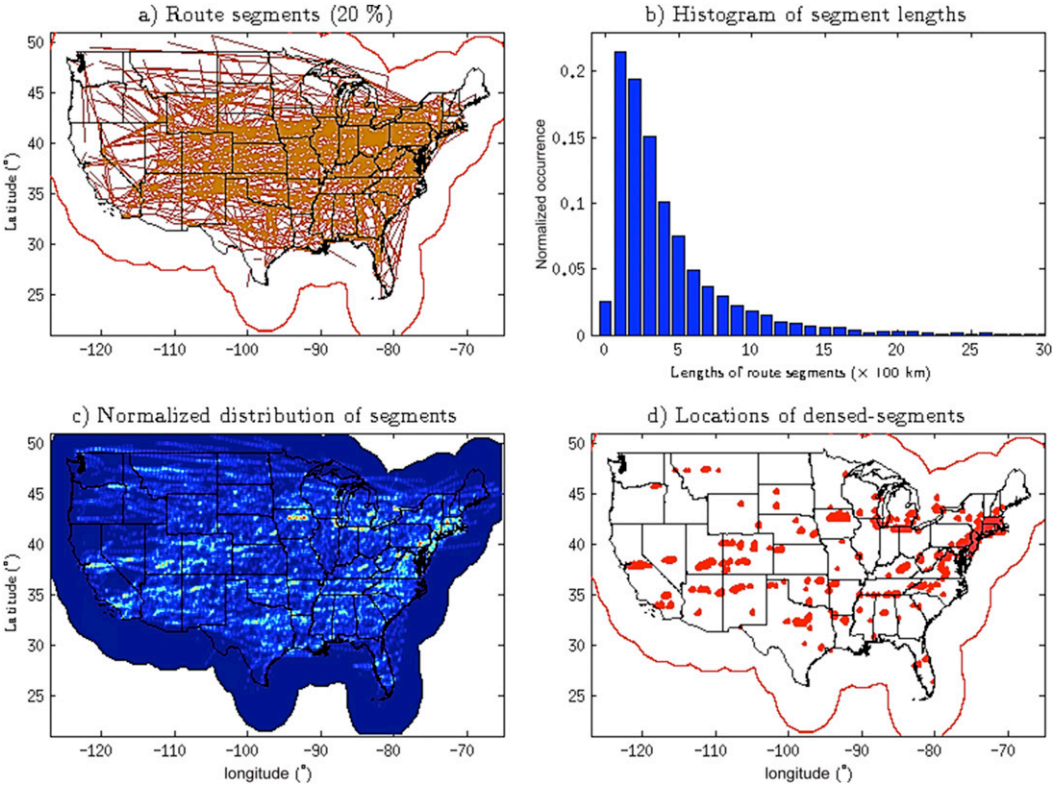

FIG. 4. (a) Route-based segments (20% of 6981; otherwise, they are clustered, making it hard to show the segments) in the CONUS within the area of WSR-88D coverage (estimated as a 460-km radius from the locations of the WSR-88Ds). (b) Histogram of normalized occurrence of the lengths of the segments. (c) Normalized concentration of route-based segments. (d) Locations of dense routes represented as red dots (normalized distribution ≥0.5).

approach, a hit is defined when forecast convection is located within 20 km of observed convection (solid green circles in Fig. 3a). A miss is where there is no forecast convection within 20 km of observed convection. A false alarm is defined as a forecast for convection but no observed convection within 20 km (solid red circles in Fig. 3a). Finally, a correct null is when convection is neither forecast nor observed within 20 km (see Fig. 3a). This methodology for computing neighborhood-based contingency table elements follows that of Clark et al. (2010).

The second evaluation method is the route-based segments (RO-seg) method. Routes are obtained from a list of 26 606 preferable routes in the database of National Airspace System Resources (NASR; https://nfdc.faa.gov/xwiki/bin/view/NFDC/56+Day+NASR+Subscription). Each route is an ordered set of waypoints (37 736 points in CONUS) from the departure airport to the arrival airport. Segments consist of two waypoints of which the average length is 439.65 km with a standard deviation of 489.65 km. There are 6981 segments in preferred routes when overlapped segments are excluded and they are used as route-based segments. Based on the guidelines for horizontal spacing from the FAA, airplanes should be at least 3–5 nautical miles (n mi; 1 n mi = 1.852 km) apart depending on the altitude in order to avoid wake turbulence (Alix et al. 2005). In this study, a 10 n mi wide (5 n mi from the airplane) jetway is considered. Taking the width of the jetway into account, if there is a convective pixel (18-dBZ echo-top height over 9 km) closer than 10 km (to the line linking two waypoints), then the segment in the route is determined to be closed. With this method, a hit is defined as both routes in the model forecast and observation being closed at the same segment within 20 km. A miss is the case where there is a convective pixel in the closed segment in the route in an observation but there is no convective pixel within 20 km. A false alarm is defined as a convective pixel from the route in the model forecasts that is in the closed segment but no convective pixel from an observation within 20 km. A correct null is the case when there are open segments in routes in the model forecasts and the observation (see Fig. 3b).

A histogram of route segment lengths is presented in Fig. 4b. Most of the lengths are shorter than 500 km

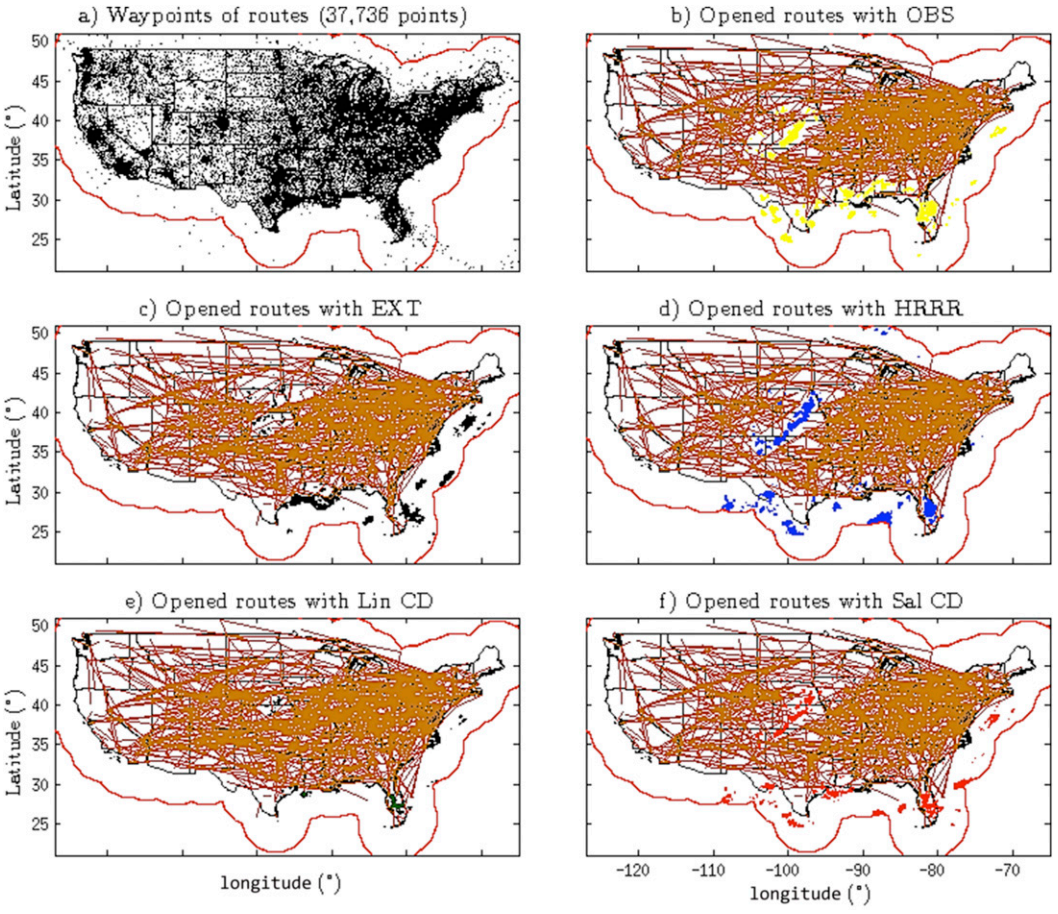

FIG. 5. (a) Waypoints (37 736 points) in the CONUS are shown as black dots. The red contour shows the area of WSR-88D coverage. (b) Open routes are shown as brown lines. The route segments are closed if an observed 18-dBZ echo-top height exceeded 9 km (yellow-filled contours; data are from 2200 UTC 8 Jun 2013) within 10 km (or half the width) of the route. Note that only 20% of opened route segments are represented. (c) As in (b), but for 18-dBZ echo-top heights exceeding 9 km based on EXT (black-filled contours). (d) As in (b), but for 18-dBZ echo-top heights exceeding 9 km based on HRRR (blue-filled contours). (e) As in (b), but for 18-dBZ echo-top heights exceeding 9 km based on Lin CD (green-filled contours). (f) As in (b), but for 18-dBZ echo-top heights exceeding 9 km based on Sal CD (red-filled contours).

(Fig. 4b). The route segments are interpolated onto a two-dimensional array and counted to obtain numbers of overlaid segments in each pixel and normalized (Fig. 4c). Dense routes are defined as the normalized number of overlaid segments ≥ 0.5 (Fig. 4d). The routes are not distributed uniformly across the CONUS, as shown in Figs. 4c and 4d. The routes are denser in the northeast and there are more east–west-oriented routes than north–south paths. To illustrate the RO-seg method for a specific case, open route segments are depicted as brown lines in Fig. 5. Compared to the NE method, the RO-seg method is advantageous for aviation applications because it only considers areas within flight routes.

Contingency tables (Wilks 2011) of neighborhood and RO-seg methods are constructed from the cumulative hits a, misses b, false alarms c, and correct rejections d at each forecast hour from all 24 cases. From the contingency tables, the probability of detection (POD), false alarm ratio (FAR), bias, and equitable threat score (ETS) are calculated using the equations below:

$$\mathrm{POD} = \frac{a}{a+b}, \tag{5}$$

$$\mathrm{FAR} = \frac{c}{a+c}, \tag{6}$$

$$\mathrm{bias} = \frac{a+c}{a+b}, \quad \text{and} \tag{7}$$

$$\mathrm{ETS} = \frac{a-c_h}{a+b+c-c_h}, \tag{8}$$

where c_h is the number of hits expected by chance and is calculated as $c_h = (a+b)(a+c)/a+b+c+d$. Bias

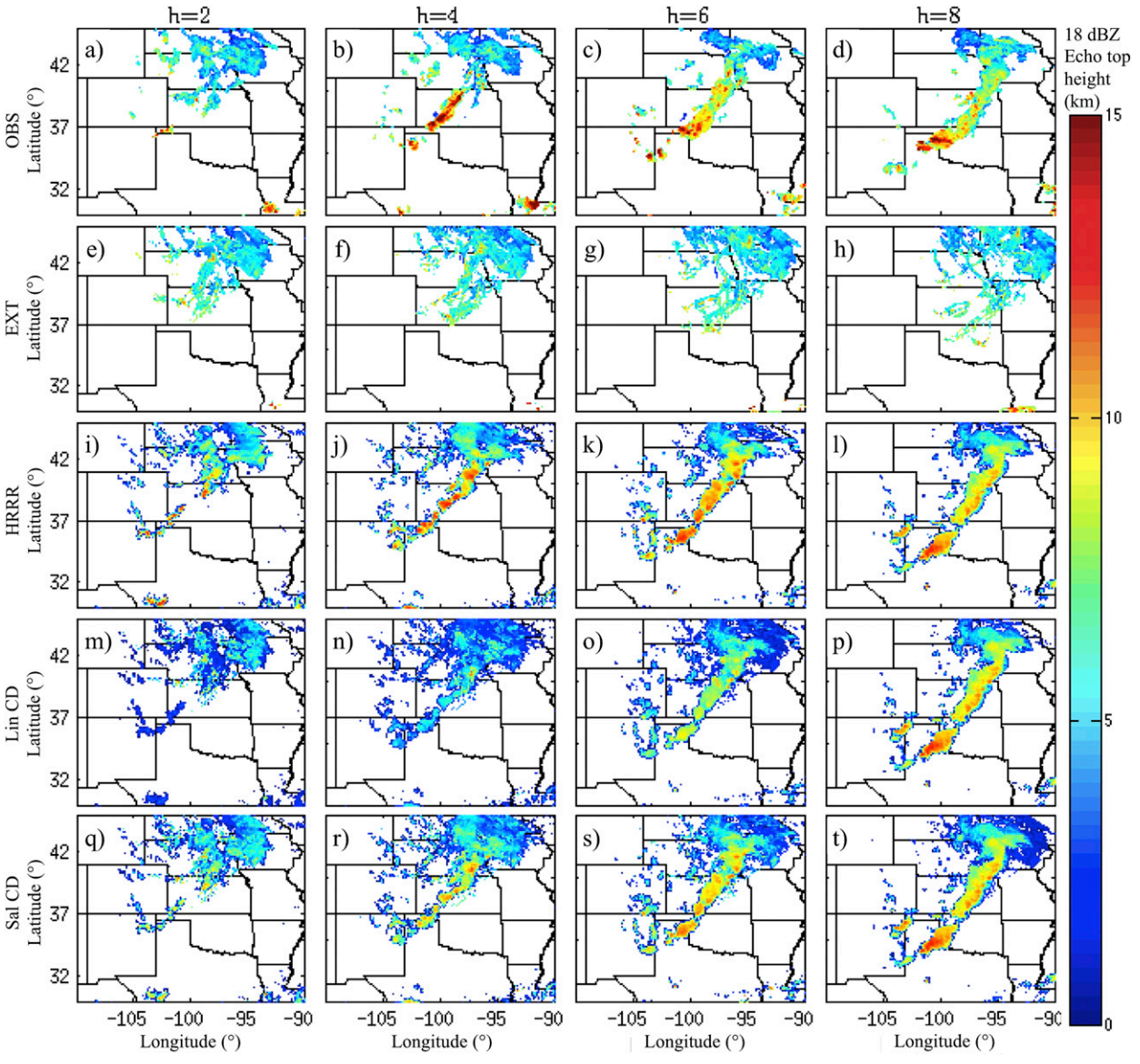

FIG. 6. Examples of echo-top heights (a)–(d) observed and forecasted by (e)–(h) EXT, (i)–(l) HRRR, (m)–(p) Lin CD, and (q)–(t) Sal CD at selected forecast times of 2, 4, 6, and 8 h using the data on 8 Jun 2013.

indicates whether the forecast under- (<1) or overestimates (>1) areal coverage with a perfect score of 1. The ETS measures the portion of observed and/or forecast events that were correctly predicted and is adjusted for hits associated with random chance. The ETS has a range of from $-\frac{1}{3}$ to 1 with a perfect score of 1 and assigns negative values for an unskilled forecast. Previous studies (e.g., Hamill 1999) point out that comparisons of ETS from competing forecasts may be misleading if their biases are different. Thus, in some cases it is important to apply a bias adjustment to equalize the biases of the competing systems and obtain a more equitable comparison. Herein, a bias adjustment is applied to the results presented in section 3.

f. Determination of statistical significance

The resampling methodology described by Hamill (1999) is applied to determine whether differences in ETS between the Sal CD forecasts and the other sets of forecasts are statistically significant. For each set of comparisons at each forecast hour, resampling was repeated 10 000 times. For application to this study, the Hamill (1999) method involves computing a test statistic using the difference in ETS between Sal CD and the forecast to which it is compared. Then, a distribution of

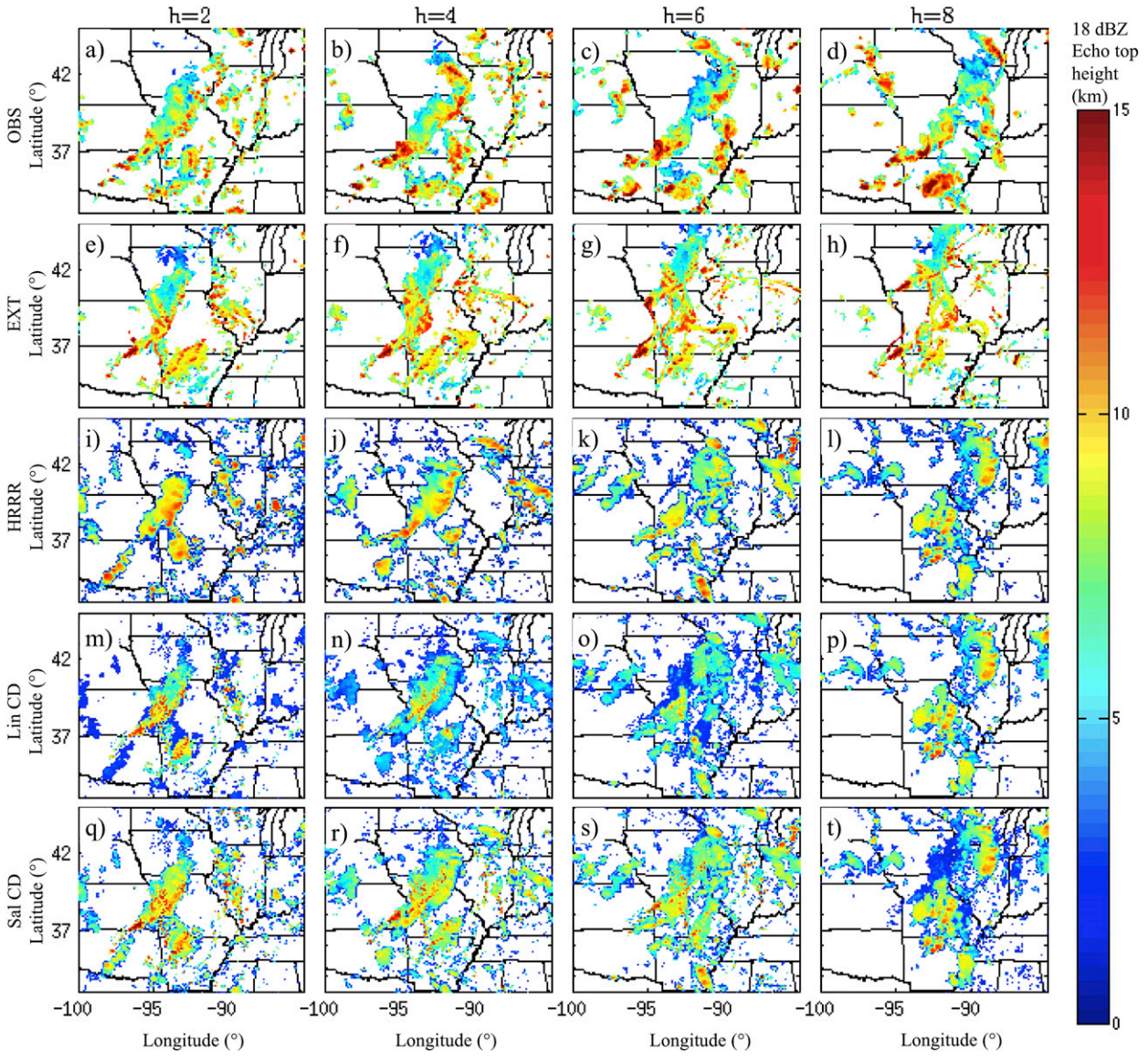

FIG. 7. As in Fig. 6, but for the data on 30 May 2013.

resampled test statistics is created by randomly choosing the Sal CD or other forecast for each case and then summing the contingency table elements over all cases. The location of the test statistic with the distribution of the resampled test statistics determines whether the differences are statistically significant.

3. Results

a. Example case 1

To illustrate qualitatively the typical performance characteristics of the various forecasting methods, a representative case with forecasts initialized at 1800 UTC 8 June 2013 is presented in Fig. 6. The synoptic weather regime associated with this case was characterized by an amplifying midtropospheric short-wave trough that moved southeastward from northeastern Wyoming to south-central Kansas during the period 1200–0000 UTC 8 June. Ahead of this trough at 1900 UTC, a cold front stretched from south-central Nebraska through western Kansas. As this cold front moved south and east into an increasingly unstable air mass, storms began to initiate at ~2000 UTC along the front. By 2100 UTC the storms had congealed into a line, which expanded while moving south and east. At 0200 UTC, the last forecast hour considered, a broken line of storms stretched from southwestern Iowa, through eastern Kansas, into

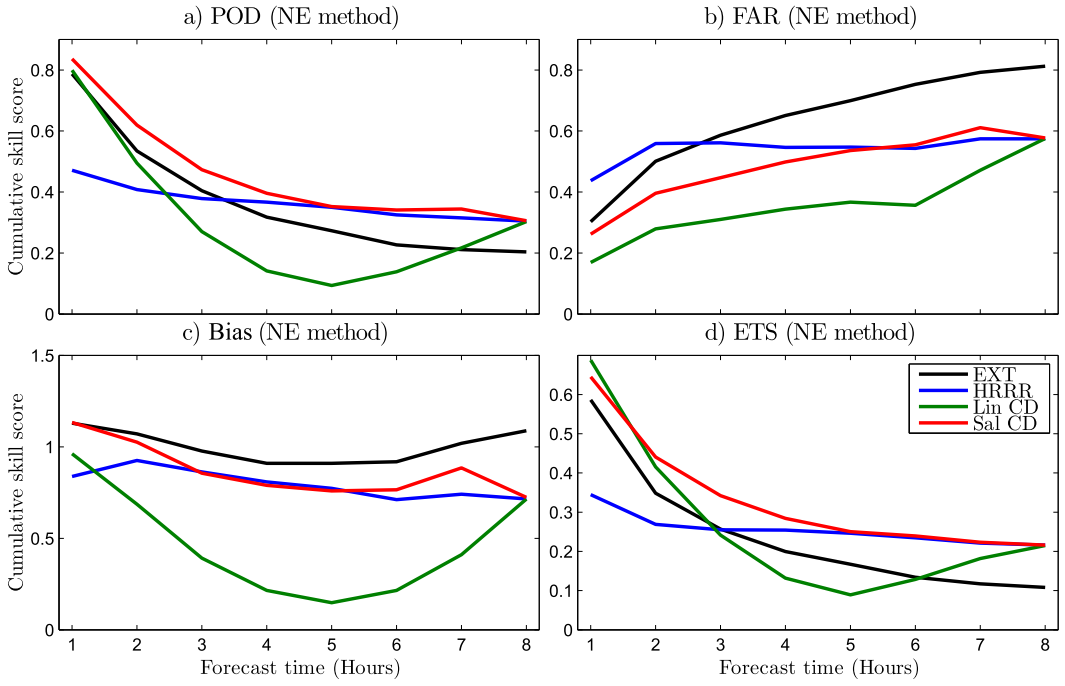

FIG. 8. Using the 20-km-radius NE method from EXT (black line), HRRR (blue line), Lin CD (green line), and Sal CD (red line) for forecasts over 24 days from mid-May to mid-June 2013, results of (a) POD, (b) FAR, (c) bias, and (d) ETS.

northwestern Oklahoma, and to the Texas Panhandle. The storms at the southern end of the line in the Texas Panhandle were the most intense.

The hourly forecasts and corresponding observations of 18-dBZ echo-top heights for this case are shown in Fig. 6. According to the observations, a strong squall line with high echo-top heights developed in central Kansas and moved to the east. The extrapolation captures the movements of cells present at the starting time properly, but does not show the development of this strong storm cell. HRRR depicts the strong storm cell throughout the time clearly after 3 h. Lin CD captures the features from EXT and HRRR; however, the intensities are underestimated compared to observations. Sal CD shows the best results compared to earlier times of HRRR and later times of EXT and all of Lin CD. Sal CD captures the features from EXT and HRRR by showing the development and the movement of the center cell successfully. Compared to the results of Lin CD, Sal CD shows better results by keeping the intensities from HRRR and adding more information at 8 h.

b. *Example case 2*

To illustrate another representative case, forecasts initialized at 1800 UTC 30 May 2013 are presented in Fig. 7. In this case, the synoptic-scale forcing was characterized by a cutoff low in the midtroposphere situated in northeastern Wyoming and an attendant negatively tilted trough moving northeast across the southern plains of Kansas, Oklahoma, and Texas into Missouri and Arkansas. Sufficient moisture and vertical wind shear were present to support severe weather and organized deep moist convection. At the surface, a cold front stretched from western South Dakota through western Nebraska, Kansas, and north of New Mexico ahead of the trough at 0600 UTC, and moved slowly to the east. As this cold front stretched farther south and east into an increasingly unstable air mass, storms began to initiate at about 0800 UTC along the front. By 1600 UTC the storms had congealed into a line, which expanded while moving north and east. At 1800 UTC, the first forecast hour considered, a broken line of storms stretched from the middle Mississippi valley, through southeastern Kansas, into central Oklahoma. The storms at the southern end of the line near the borders of Oklahoma, Kansas, Arkansas, and Missouri maintained the strongest intensities. It should be noted that the northern part of the line in Illinois weakened after 0200 UTC 31 May and the storms south of the line redeveloped in central Arkansas at the same time.

The hourly forecasts and corresponding observations of 18-dBZ echo-top heights for this case are shown in Fig. 7. According to the observations, a strong previously developed squall line with high echo-top heights

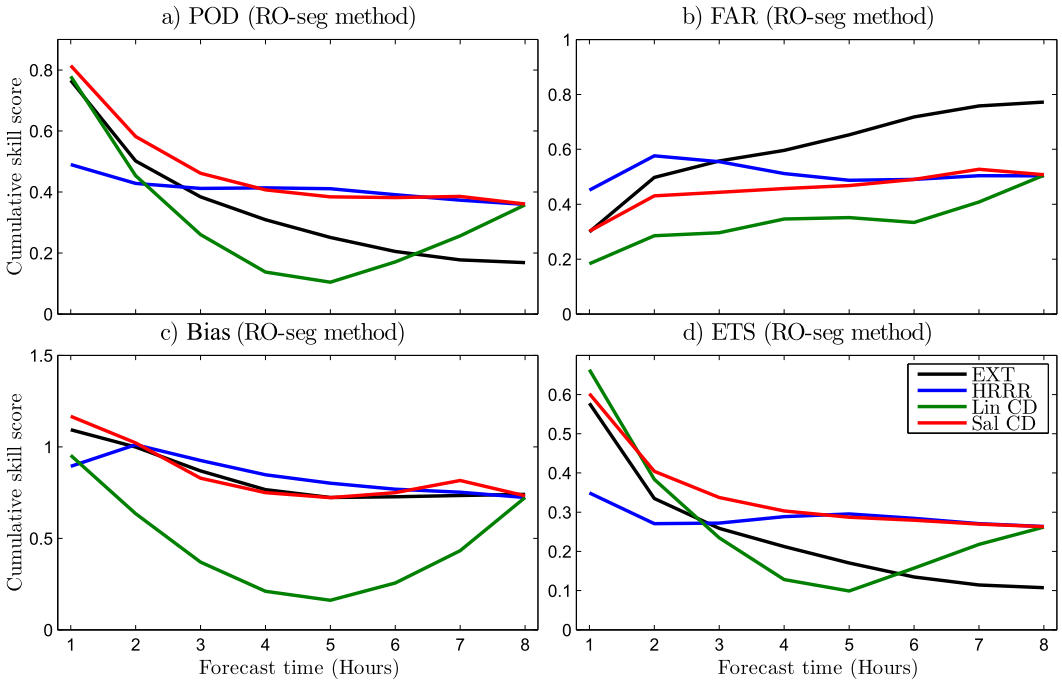

FIG. 9. As in Fig. 8, but for the 10-km route-based segments method.

from the middle Mississippi valley to central Oklahoma moved to the east. The EXT captures the movements of cells present at the starting time properly, but does not show the redevelopment of the strong storm cells in central Arkansas. HRRR depicts the features of the squall line throughout the forecast but the location is displaced and intensities are lower compared to the observations and EXT. However, HRRR shows redeveloping storm cells in southwestern Arkansas (located in central Arkansas in the observations). Because of lower intensities and displacements in HRRR, Lin CD and Sal CD do not show better performance compared to the EXT at 4–8 h in this particular case. However, Sal CD shows the best results up to 3 h by capturing the features from EXT and HRRR. The poor performance of Sal CD at later hours reflects the strong dependence on the HRRR forecast at these hours. Thus, if the HRRR forecasts are poor, the Sal CD forecasts will also be poor.

c. *Statistical evaluation*

Values of POD, FAR, bias, and ETS computed from contingency table elements defined using a 20-km radius for EXT (black line), HRRR (blue line), Lin CD (green line), and Sal CD (red line) computed at each forecast hour over the 24 cases are shown in Fig. 8. The skill of EXT quickly drops with increasing forecast lead time and EXT performs better than HRRR until 3 h. HRRR skill scores drop slightly with increasing lead time, but in general remain more constant than the other forecasts. Lin CD generally performs worse than EXT and HRRR from 3 to 6 h, while Sal CD performs best overall with respect to POD and ETS. It should be noted that Lin CD has very low bias (<0.3) especially from 4 to 6 h (i.e., underestimation). Sal CD performs particularly well relative to the other forecasts during the 2–5-h lead times. The largest differences in ETS and POD between Sal CD and the other forecasts coincides within the time that ETS and POD from EXT and HRRR cross, which indicates that, instead of utilizing EXT and HRRR individually, combining those data can improve the forecast.

Skill scores of POD, FAR, bias, and ETS using the RO-seg method averaged over the 24 days are shown in Fig. 9. The skill scores are similar to that of the NE method; however, the ETS of Sal CD converges to that of HRRR at 4 h (it converged at 5 h for the NE method). The ETS of HRRR using the RO-seg method shows better results than the NE method from 3 to 8 h, which is likely related to the RO-seg method considering a more restricted area compared to the NE method.

Because bias can impact comparisons of ETS by sometimes giving the forecast with a higher bias an artificially inflated score, a bias correction procedure is applied following methods similar to those in Jenkner et al. (2008) and Clark et al. (2011). The corrections are only applied to EXT, HRRR, and Sal CD. Lin CD is excluded from bias correction because at some forecast

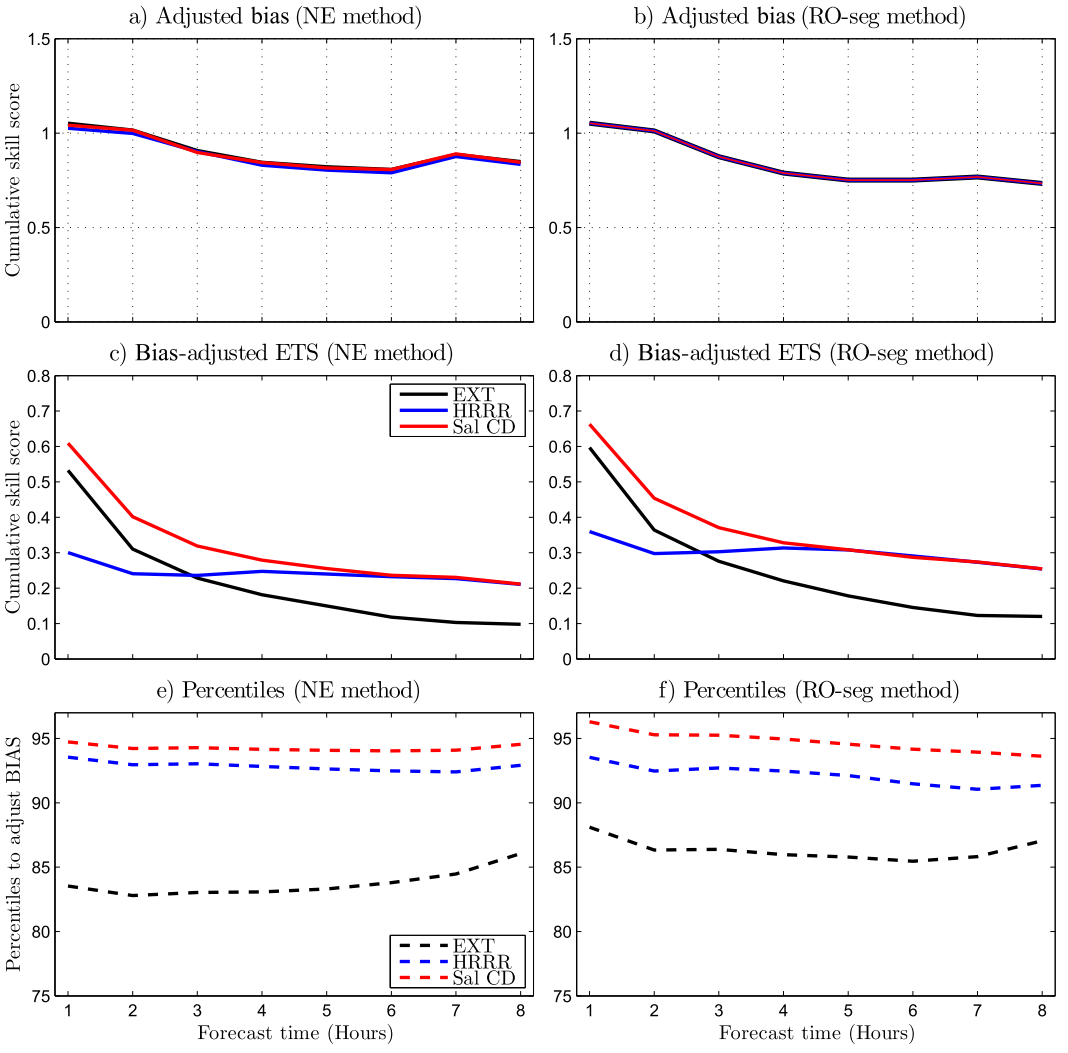

FIG. 10. (a) Adjusted bias computed using the 20-km-radius NE method of EXT (black line), HRRR (blue line), and Sal CD (red line) for forecasts over 24 days from mid-May to mid-June 2013. (b) As in (a), but for the RO-seg method. (c) Bias-adjusted ETS using the NE method. (d) As in (c), but for the RO-seg method. (e) Percentiles of EXT, HRRR, and Sal CD to correct bias based on areal coverage of 9-km observations using the NE method. (f) As in (e), but for the RO-seg method.

hours, especially the 3–6-h range, biases were as low as 0.25 (Fig. 8c) and correcting for the bias would have resulted in a drastically different appearing forecast. Biases for Sal CD, EXT, and HRRR were all clustered around 1; thus, the bias correction only results in a minor adjustment to the forecasts that serves to make the ETS comparisons more equitable.

The bias correction is applied by finding the average bias of Sal CD, EXT, and HRRR at each forecast hour. Then, using the distribution of 18-dBZ echo-top heights, a new threshold that gives the average bias is computed. The new thresholds are slightly different among the three sets of forecasts, but have the same areal coverage and, thus, the ETSs computed from these new thresholds are not impacted by differences in bias. The bias-corrected comparisons are shown in Fig. 10.

d. Statistical significance

Using the methodology of Hamill (1999), distributions of differences in resampled ETS at each forecast time are calculated and the range between the 2.5th and 97.5th percentiles of these distributions is used to illustrate statistically significant differences. Those ranges are represented as error bars in Fig. 11. If the compared forecasts are outside of the range of error bars, the improvement is significant.

In the comparisons between Sal CD and EXT (Figs. 11a,b), the Sal CD scores are significantly better

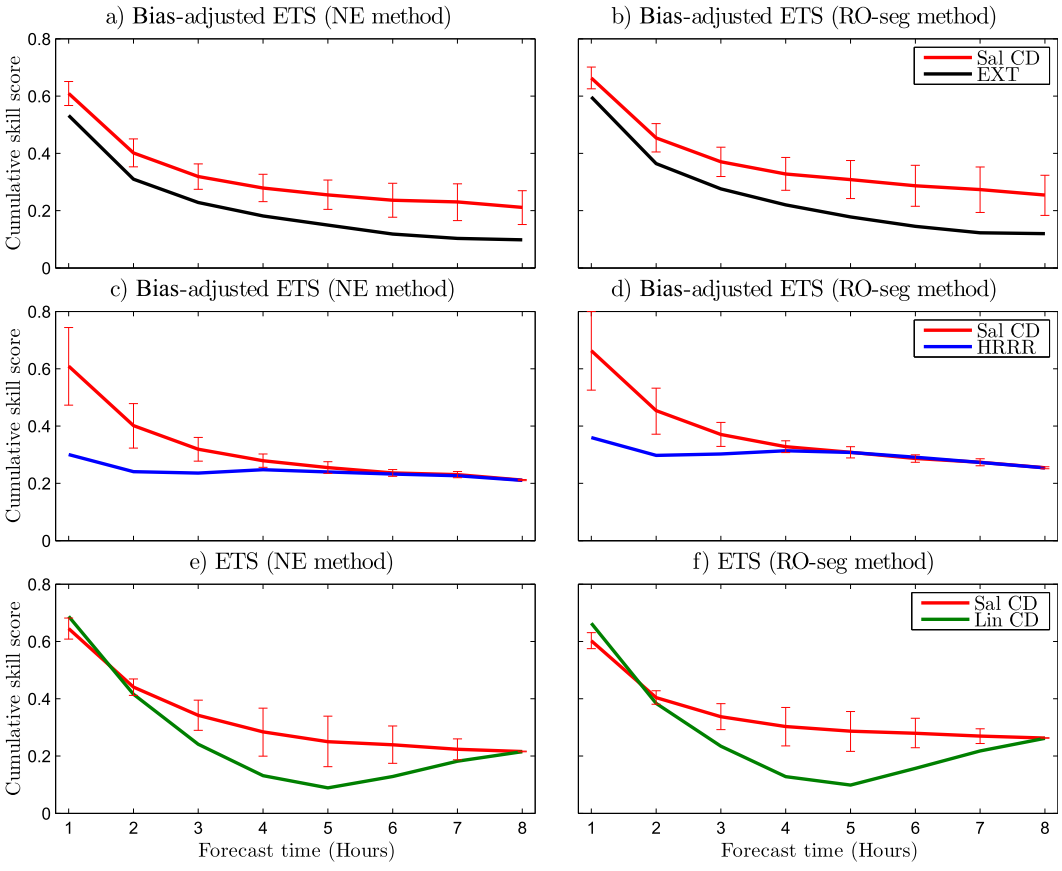

FIG. 11. (a) Bias-adjusted ETS computed using the 20-km-radius NE method of EXT (black line) and Sal CD (red line) with error bars showing the 2.5th and 97.5th percentiles of differences (10 000 resamples) between ETS computed with Sal CD and with EXT. (b) As in (a), but for differences from EXT when using the RO-seg method. (c) As in (a), but for differences when using HRRR. (d) As in (b), but for differences from EXT when using HRRR. (e) As in (a), but for differences from ETS (not bias-adjusted ETS) computed from Lin CD. (f) As in (e), but for differences from Lin CD using the RO-seg method.

than those for EXT at all forecast hours. In the Sal CD and HRRR comparisons (Figs. 11c,d), Sal CD has significantly better scores up until forecast hour 4 using the NE method and until forecast hour 3 using the RO-seg method, after which the scores begin to converge. Finally, for the Sal CD and Lin CD comparisons (Figs. 11e,f), Lin CD is significantly better at forecast hour 1 for both the NE and RO-seg methods, while Sal CD is significantly better at forecast hours 3–7 using both methods.

4. Summary and future work

a. Summary

A new technique to blend extrapolation and model forecasts was developed and evaluated using observations and forecasts over 24 days from mid-May to mid-June 2013. In general, blending techniques using weighted averaging apply constant weights for both extrapolation (w) and model forecasts ($1 - w$) at each forecast lead time. For example, $w = 1$ is applied to the extrapolation and $1 - w = 0$ is applied to the model forecast at the beginning of the forecast and w decreases gradually to $w = 0$ at the end of the forecast. The weighted averaging (linear cross dissolve) has a problem producing underestimated blended values during the middle of the forecast, where both w and $1 - w$ are close to 0.5 if the forecasts are displaced. To mitigate this problem, the model forecast and extrapolation fields can be aligned before weights are applied; however, displacements remain even after this alignment. To further improve the blending results, a technique called salient cross dissolve is applied in this work. Two-dimensional weights w_s based on the differences between normalized intensities from the extrapolation and model forecast are determined for each forecast hour (as a function of time fraction w). The novelty of salient cross dissolve is

in preserving the values in both the extrapolation and model forecasts if they are high enough. For example, if there are two convective cells in both extrapolation and model forecasts in the middle of forecast lead time, salient cross dissolve tends to shrink the cells by applying different weights (i.e., higher weights are applied to higher values and lower weights are applied to lower values, which preserves most of the high-valued pixels and eliminates many of the low-valued pixels) while linear cross dissolve cuts every value in half. Salient cross dissolve showed better results than those of linear cross dissolve in this study. Instead of fading out in linear cross dissolve, w_s enables the pixels with strong intensities to be preserved in salient cross dissolve, resulting in more pixels with higher values.

For the forecast evaluations, a new method called the route-based segments method, which considers airplane routes, was developed and tested with comparisons made to a neighborhood-based method. Both methods gave very similar results indicating superior performance for the forecasts using salient cross dissolve, particularly during forecast hours 2–5 h.

b. Future work

The contribution of the work is adding additional information to the weights applied to the extrapolations and the model forecasts. Considering differences of normalized intensities showed promising results and helped give more realistic intensities in blended forecasts. Instead of adjusting values in model forecasts based on linear weights that vary as a function of time, salient cross dissolve also considers intensities so that pixels with high values are retained. However, updated weights (i.e., w_s) do not reflect actual data from the extrapolation nor model forecasts. Future studies should consider the processes of adjusting those weights considering the real data and past performance. Additionally, frequently updating extrapolation, in other words, adding latest observational information at 15-min time intervals, should be utilized. Finally, it is also possible to consider weights as two separate variables instead of using w_s and $1 - w_s$. The independent variables can be adjusted using machine learning. Updated techniques using such methods are planned for future applications.

Acknowledgments. Funding for the authors was provided by the NOAA/National Weather Service (NWS) Next Generation Air Transportation System (NextGen) weather program to the NOAA/Office of Oceanic and Atmospheric Research under NOAA–OU Cooperative Agreement NA11OAR4320072, U.S. Department of Commerce. The techniques described in this paper have been implemented within the Warning Decision Support System–Integrated Information (WDSS-II; Lakshmanan and Smith 2007) as the tool w2morphtrack. We thank Eric P. Jacobsen for help proofreading, Jason Levit and Mark Miller for useful suggestions on the tools developed herein, and Steven Lack at the NOAA Aviation Weather Center for information on aviation forecasting needs of the FAA.

REFERENCES

Alix, D. C., P. D. Simich, H. Wassaf, and F. Y. Wang, 2005: Acoustic characterization of wake vortices in ground effect. *Proc. 43rd Aerospace Sciences Meeting and Exhibit*, Reno, NV, AIAA 2005-260.

Brown, J. M., and Coauthors, 2011: Improvement and testing of WRF physics options for application to Rapid Refresh and High Resolution Rapid Refresh. *Proc. 15th Conf. on Aviation, Range, and Aerospace Meteorology*, Los Angeles, CA, Amer. Meteor. Soc., 5.5. [Available https://ams.confex.com/ams/14Meso15ARAM/webprogram/Paper191234.html.]

Chou, M.-D., and M. J. Suarez, 1994: An efficient thermal infrared radiation parameterization for use in general circulation models. NASA Tech. Memo. 104606, Technical Report Series on Global Modeling and Data Assimilation, Vol. 3, 85 pp. [Available online at http://gmao.gsfc.nasa.gov/pubs/docs/Chou128.pdf.]

Clark, A. J., W. A. Gallus Jr., and M. L. Weisman, 2010: Neighborhood-based verification of precipitation forecasts from convection-allowing NCAR WRF Model simulations and the operational NAM. *Wea. Forecasting*, **25**, 1495–1509, doi:10.1175/2010WAF2222404.1.

——, and Coauthors, 2011: Probabilistic precipitation forecast skill as a function of ensemble size and spatial scale in a convection-allowing ensemble. *Mon. Wea. Rev.*, **139**, 1410–1418, doi:10.1175/2010MWR3624.1.

Dixon, M., and G. Wiener, 1993: TITAN: Thunderstorm Identification, Tracking, Analysis, and Nowcasting—A radar-based methodology. *J. Atmos. Oceanic Technol.*, **10**, 785–797, doi:10.1175/1520-0426(1993)010<0785:TTITAA>2.0.CO;2.

Dupree, W., and Coauthors, 2009: The advanced storm prediction for aviation forecast demonstration. *WMO Symp. on Nowcasting*, Whistler, BC, Canada, WMO.

Fahey, T. H., T. Phaneuf, W. S. Leber, M. Huberdeau, D. P. Morin, and D. Sims, 2006: Forecasts of convection for air traffic management strategic decision making: Comparison of user needs and available products. Preprints, *12th Conf. on Aviation, Range, and Aerospace Meteorology*, Atlanta, GA, Amer. Meteor. Soc., 2.4. [Available online at https://ams.confex.com/ams/pdfpapers/105165.pdf.]

Germann, U., and I. Zawadzki, 2002: Scale-dependence of the predictability of precipitation from continental radar images. Part I: Description of the methodology. *Mon. Wea. Rev.*, **130**, 2859–2873, doi:10.1175/1520-0493(2002)130<2859:SDOTPO>2.0.CO;2.

——, and ——, 2004: Scale dependence of the predictability of precipitation from continental radar images. Part II: Probability forecasts. *J. Appl. Meteor.*, **43**, 74–89, doi:10.1175/1520-0450(2004)043<0074:SDOTPO>2.0.CO;2.

Grundland, M., R. Vohra, G. P. Williams, and N. A. Dodgson, 2006: Cross dissolve without cross fade: Preserving contrast, color and salience in image compositing. *Comput. Graphics Forum*, **25**, 577–586, doi:10.1111/j.1467-8659.2006.00977.x.

Hamill, T. M., 1999: Hypothesis tests for evaluating numerical precipitation forecasts. *Wea. Forecasting*, **14**, 155–167, doi:10.1175/1520-0434(1999)014<0155:HTFENP>2.0.CO;2.

Huang, X.-Y., and P. Lynch, 1993: Diabatic digital-filtering initialization: Application to the HIRLAM model. *Mon. Wea. Rev.*, **121**, 589–603, doi:10.1175/1520-0493(1993)121<0589:DDFIAT>2.0.CO;2.

Jenkner, J., C. Frei, and C. Schwierz, 2008: Quantile-based short-range QPF evaluation over Switzerland. *Meteor. Z.*, **17**, 827–848, doi:10.1127/0941-2948/2008/0344.

Lakshmanan, V., and T. Smith, 2007: The Warning Decision Support System–Integrated Information. *Wea. Forecasting*, **22**, 596–612, doi:10.1175/WAF1009.1.

——, and ——, 2010: An objective method of evaluating and devising storm-tracking algorithms. *Wea. Forecasting*, **25**, 701–709, doi:10.1175/2009WAF2222330.1.

——, R. Rabin, and V. DeBrunner, 2003: Multiscale storm identification and forecast. *J. Atmos. Res.*, **67–68**, 367–380, doi:10.1016/S0169-8095(03)00068-1.

——, T. Smith, K. Hondl, G. J. Stumpf, and A. Witt, 2006: A real-time, three-dimensional, rapidly updating, heterogeneous radar merger technique for reflectivity, velocity, and derived products. *Wea. Forecasting*, **21**, 802–823, doi:10.1175/WAF942.1.

——, K. Hondl, and R. Rabin, 2009: An efficient, general-purpose technique for identifying storm cells in geospatial images. *J. Atmos. Oceanic Technol.*, **26**, 523–537, doi:10.1175/2008JTECHA1153.1.

——, ——, C. K. Potvin, and D. Preignitz, 2013: An improved method for estimating radar echo-top height. *Wea. Forecasting*, **28**, 481–488, doi:10.1175/WAF-D-12-00084.1.

Li, L., W. Schmid, and J. Joss, 1995: Nowcasting of motion and growth of precipitation with radar over a complex orography. *J. Appl. Meteor.*, **34**, 1286–1300, doi:10.1175/1520-0450(1995)034<1286:NOMAGO>2.0.CO;2.

Lin, C., S. Vasić, A. Kilambi, B. Turner, and I. Zawadzki, 2005: Precipitation forecast skill of numerical weather prediction models and radar nowcasts. *Geophys. Res. Lett.*, **32**, L14801, doi:10.1029/2005GL023451.

Mandapaka, P. V., U. Germann, L. Panziera, and A. Hering, 2012: Can Lagrangian extrapolation of radar fields be used for precipitation nowcasting over complex alpine orography? *Wea. Forecasting*, **27**, 28–49, doi:10.1175/WAF-D-11-00050.1.

Matthews, M., and R. DeLaura, 2010: Assessment and interpretation of en route weather avoidance fields from the convective weather avoidance model. *Proc. 10th AIAA Aviation Technology, Integration, and Operations (ATIO) Conf.*, Fort Worth, TX, AIAA 2010-9160.

Mlawer, E. J., S. J. Taubman, P. D. Brown, M. J. Iacono, and S. A. Clough, 1997: Radiative transfer for inhomogeneous atmospheres: RRTM, a validated correlated-*k* model for the longwave. *J. Geophys. Res.*, **102**, 16 663–16 682, doi:10.1029/97JD00237.

Nakanishi, M., and H. Niino, 2004: An improved Mellor–Yamada level-3 model with condensation physics: Its design and verification. *Bound.-Layer Meteor.*, **112**, 1–31, doi:10.1023/B:BOUN.0000020164.04146.98.

Pinto, J., W. Dupree, S. Weygandt, M. Wolfson, S. Benjamin, and M. Steiner, 2010: Advances in the Consolidated Storm Prediction for Aviation (CoSPA). Preprints, *14th Conf. on Aviation, Range, and Aerospace Meteorology*, Atlanta, GA, Amer. Meteor. Soc., J11.2. [Available online at https://ams.confex.com/ams/pdfpapers/163811.pdf.]

Robinson, M., W. Moser, and J. Evans, 2008: Measuring the utilization of available aviation system capacity in convective weather. Preprints, *13th Conf. on Aviation, Range, and Aerospace Meteorology*, New Orleans, LA, Amer. Meteor. Soc., 3.3. [Available online at https://ams.confex.com/ams/pdfpapers/132957.pdf.]

Sasaki, Y., 1958: An objective analysis based on the variational method. *J. Meteor. Soc. Japan*, **36**, 77–88.

——, 1970: Some basic formalisms in numerical variational analysis. *Mon. Wea. Rev.*, **98**, 875–883, doi:10.1175/1520-0493(1970)098<0875:SBFINV>2.3.CO;2.

Sheth, K., T. Amis, S. Gutierrez-Nolasco, B. Spridhar, and D. Mulfinger, 2013: Development of a probabilistic convective weather forecast threshold parameter for flight-routing decisions. *Wea. Forecasting*, **28**, 1175–1187, doi:10.1175/WAF-D-12-00052.1.

Skamarock, W., and Coauthors, 2008: A description of the Advanced Research WRF Version 3. NCAR Tech. Note NCAR/TN–475+ STR, 113 pp. [Available online at http://www2.mmm.ucar.edu/wrf/users/docs/arw_v3.pdf.]

Smirnova, T., J. Brown, and S. Benjamin, 1997: Evolution of soil moisture and temperature in the MAPS/RUC assimilation cycle. Preprints, *13th Conf. on Hydrology*, Long Beach, CA, Amer. Meteor. Soc., 172–175.

Song, L., C. Wanke, D. Greenbaum, S. Zobell, and C. Jackson, 2008: Methodologies for estimating the impact of severe weather on airspace capacity. *Proc. 26th Int. Congress of the Aeronautical Sciences*, Anchorage, AK, AIAA 2008-8917.

Stratman, D. R., M. C. Coniglio, S. E. Koch, and M. Xue, 2013: Use of multiple verification methods to evaluate forecasts of convection from hot- and cold-start convection-allowing models. *Wea. Forecasting*, **28**, 119–138, doi:10.1175/WAF-D-12-00022.1.

Sun, J., and Coauthors, 2014: Use of NWP for nowcasting convective precipitation: Recent progress and challenges. *Bull. Amer. Meteor. Soc.*, **95**, 409–426, doi:10.1175/BAMS-D-11-00263.1.

Thompson, G., P. R. Field, R. M. Rasmussen, and W. D. Hall, 2008: Explicit forecasts of winter precipitation using an improved bulk microphysics scheme. Part II: Implementation of a new snow parameterization. *Mon. Wea. Rev.*, **136**, 5095–5115, doi:10.1175/2008MWR2387.1.

Weygandt, S. S., and Coauthors, 2011: Evaluation of the National Centers for Environmental Prediction (NCEP) implementation version of the Rapid Refresh and its skill in providing short-term guidance for aviation hazards. *Proc. 15th Conf. on Aviation, Range, and Aerospace Meteorology*, Los Angeles, CA, Amer. Meteor. Soc., 5.4. [Available online at https://ams.confex.com/ams/14Meso15ARAM/webprogram/Paper191213.html.]

Wilks, D. S., 2011: *Statistical Methods in the Atmospheric Sciences*. 3rd ed. Elsevier, 676 pp.

Wolfson, M. M., W. J. Dupree, R. M. Rasmussen, M. Steiner, S. G. Benjamin, and S. S. Weygandt, 2008: Consolidated storm prediction for aviation (CoSPA). *Integrated Communications, Navigation and Surveillance Conference*, Bethesda, MD, IEEE, 1–19, doi:10.1109/ICNSURV.2008.4559190.